Selective carrier injection into patterned arrays of pyramidal quantum dots for entangled photon light-emitting diodes

T. H. Chung[†], G. Juska[*][†], S. T. Moroni, A. Pescaglini, A. Gocalinska and E. Pelucchi

Scalability and foundry compatibility (as apply to conventional silicon-based integrated computer processors, for example) in developing quantum technologies are major challenges facing current research. Here we introduce a quantum photonic technology that has the potential to enable the large-scale fabrication of semiconductor-based, site-controlled, scalable arrays of electrically driven sources of polarization-entangled photons that may be able to encode quantum information. The design of the sources is based on quantum dots grown in micrometre-sized pyramidal recesses along the crystallographic direction (111)B, which theoretically ensures high symmetry of the quantum dots—a requirement for bright entangled-photon emission. A selective electric injection scheme in these non-planar structures allows a high density of light-emitting diodes to be obtained, with some producing entangled photon pairs that also violate Bell's inequality. Compatibility with semiconductor fabrication technology, good reproducibility and lithographic position control make these devices attractive candidates for integrated photonic circuits for quantum information processing.

To develop quantum technologies, the scientific community is looking into several alternative practical routes such as superconducting qubits, atoms on-chips and photonic integrated circuits, among others[1–4]. All of the explored technologies have to solve the scalability and reproducibility problem if they are to deliver successful real-life applications. In the case of photonic quantum technologies, scalability requires moving from discrete optical elements to integrated photonic circuits and to on-chip solid-state sources, allowing, for example, thousands of units to operate in unison—a requirement that is very hard to realize at the moment.

Semiconductor quantum dot (QD) technology is fundamentally compatible with modern fabrication/foundry processes, and on-demand identical, single and entangled photons have all been demonstrated by optical pumping[5–14]. Nevertheless, although the development of electrically pumped (EP) quantum light sources has advanced in general[15], the development of a particular resource, EP entangled photon sources, has proven more challenging. After the first report[16], the community had to wait several years before a similar result could be obtained by other groups[17]. Importantly, the few devices reported so far utilized epitaxial self-assembled QD structures, that is, these devices had no control on the source location or on the number of sources in a single device (typically hundreds or more, and not just one or, in the best case scenario, a few): a critical aspect for photonic integration scaling.

Pyramidal QD system

The technology presented herein is based on the pyramidal QD system, recently highlighted for its capability to deliver arrays of highly symmetric and uniform QDs[11,18]. The system is, nevertheless, intrinsically non-planar, a feature that has so far impeded the development of efficient electrically driven light-emitting sources. Before discussing the relevant quantum optics results, we need to highlight the complexity of the pyramidal system as a key ingredient. In short, single QDs are epitaxially grown by metalorganic vapour phase epitaxy (MOVPE) inside inverted pyramidal recesses that are lithographically patterned on a (111)B GaAs substrate (a fragment of such a template is shown in Fig. 1a). The structure comprises several differently composed III–V (Al)GaAs layers and an InGaAs QD layer (see Supplementary Information for a detailed description of each layer, and the reasons for inserting them)—all of which obey complex epitaxial dynamics as reported elsewhere[19–22]. The outcome is an ensemble of self-forming nanostructures inside each pyramidal recess, as described by the generic sketches in Fig. 1a. During the growth of an AlGaAs alloy, fast-diffusing Ga tends to segregate in the regions of the intersecting walls of the recess and in a narrow region at the centre of the pyramidal structure, effectively forming three embedded low bandgap vertical quantum wells (VQWs) and a vertical quantum wire (VQWR) of around 20 nm diameter, respectively. In addition, a thin InGaAs layer forms a group of interconnecting nanostructures: a flat QD at the central axis of the structure, three lateral quantum wires (LQWRs) and three lateral quantum wells (LQWs). This apex-down geometry hinders light extraction, which can be efficiently enhanced by two or three orders of magnitude (typically achieving a detection rate of 6×10^4–15×10^4 photons per second under continuous-wave excitation in our system) by selectively etching away the substrate (a process known as back-etching, see Methods) to obtain apex-up pyramidal structures as shown in Fig. 1b (a typical configuration used for measurements)[11,23]. The lack of planarity on both sides of a sample unfortunately prevents simply contacting the back and the top of the pyramid to fabricate a single QD light-emitting diode (LED). The proposed schematic for a micrometre-sized LED (µLED) device is depicted in Fig. 1c, emphasizing its 3D intrinsic nature and lateral dimensions of $\ll 10$ µm. The presence of a nanowire-like structure (the VQWR) running through most of the structure is also shown, and, as will be discussed later, this contributes to a selective injection process that feeds the single QD at the centre (the magnified region is shown in Fig. 1d).

Tyndall National Institute, University College Cork, Lee Maltings, Cork, Ireland. [†]These authors contributed equally to this work.
*e-mail: gediminas.juska@tyndall.ie
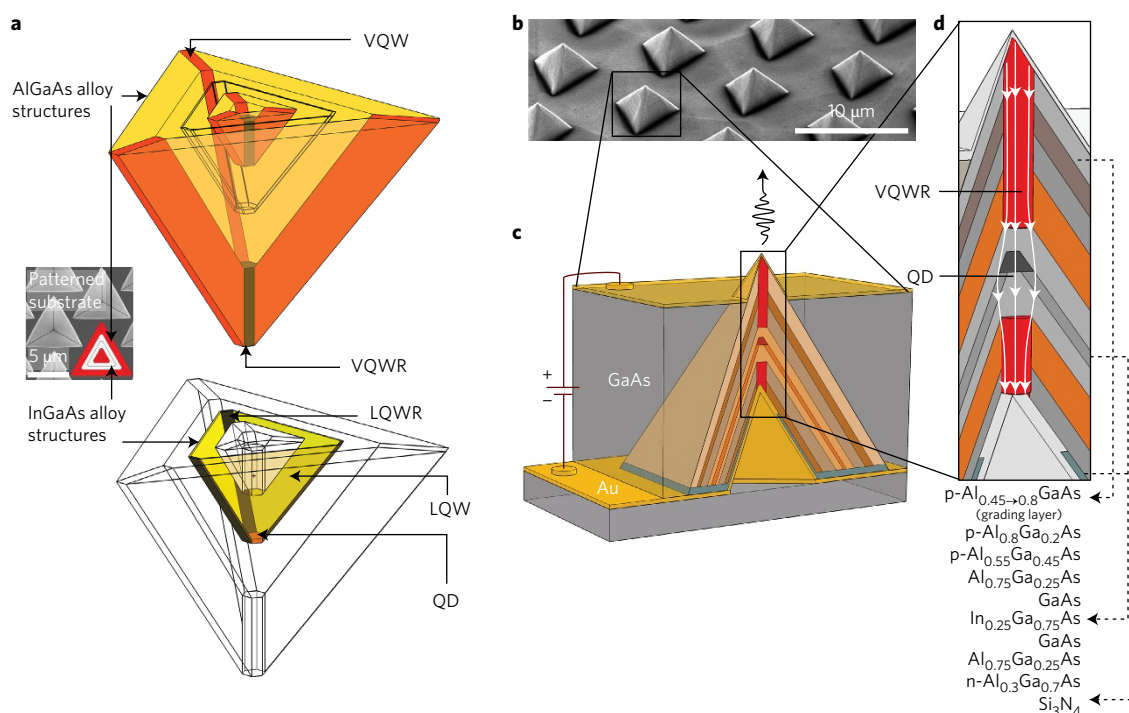
Figure 1 | The internal structure of a device and the schematics of a µLED. a, The complex ensemble of nanostructures that self-forms within the pyramidal recesses pre-etched in a GaAs substrate. The AlGaAs alloy forms Ga-enriched structures: a vertical quantum wire (VQWR) along the central axis of the pyramid, and three vertical quantum wells (VQWs). A nominally thin (0.5 nm) InGaAs alloy forms a QD, three lateral quantum wires (LQWRs) and three lateral quantum wells (LQWs). **b,** Scanning electron microscopy image of a sample right after the chemical etching step, showing the exposed pyramidal structures in an apex-up geometry that enhances light extraction by a few orders of magnitude. **c,** Sketch of a p–i–n junction µLED in cross-section view. **d,** A magnified region of the central part of a pyramid with a QD. The epitaxial layers comprise a representative structure with dominant AlGaAs alloys that form a vertical quantum wire (VQWR). Arrows indicate the injection current through the VQWR.

Selective current injection

To fabricate a QD LED, there are number of hurdles to overcome, and we will discuss the most relevant. Figure 2a shows the cross-sectional scanning electron microscopy image of the pyramidal structure, where the device is still contained inside the GaAs substrate (the grey layers result from the various Al-containing alloys and doping). The centre vertical path (blue arrow in Fig. 2a), where the single QD is located, is not the most electrically favourable path. Because of the geometry, the centre path is approximately three times longer than a short path across the side (red arrow Fig. 2a), that is, in an LED structure the current will go along the red path, resulting in a low (or no) probability of intercepting the single QD. This results in an overly crowded LED (too many charges running), impeding high-quality emission from the QD due to the spectral wandering/decoherence induced by random electric field fluctuations. Moreover, the system is even more non-ideal in its nature, presenting strong faceting at the top (this happens because there is virtually no growth on the planar (111B) substrate, resulting in 'facet crowding'; see Supplementary Information and the region circled in Fig. 2a). These lateral facets are the regions of potential current shortcuts.

To effectively achieve selective injection to the single QD, one needs to exploit a feature of the pyramidal system—the formation of the VQWR during the growth of high-bandgap $Al_{0.75}Ga_{0.25}As$ (Fig. 1a). This low-bandgap ($Al_xGa_{1-x}As$, $x \leq 0.3$) embedded nanowire is expected to act as a low-resistivity path for electrical charges to reach the InGaAs QD (that is, to introduce a low-resistivity path for charges at the centre only, while effectively leaving a high-bandgap barrier for transport in the form of the interface between $Al_{0.75}Ga_{0.25}As$ and $Al_{0.3}Ga_{0.7}As$ on the sides). To test our initial intuition, we performed finite element simulations (see Methods):

the current density distribution within the magnified region with VQWRs is shown in Fig. 2a for a simplified device model. The simulation coherently describes a preferential current path at the centre. We also observe that the VQWR does not impede the current flow to other (quantum) structures, but nevertheless most of the current is restricted to the centre region. On the basis of the simulation results, we implemented this idea in a practical device design (Fig. 1c,d).

To force current injection at the centre of a pyramid, a small Ti/Au contact must be created in that region via a couple of processing steps. First, to prevent electrical short circuits outside the region of injection, a layer of Si_3N_4 is deposited onto the as-grown sample. Second, a tilted sample is evaporated three times by Ti/Au, rotating it by 120° in the plane of sample growth each time. The resulting metallic layer acts as a mask metal, leaving a small aperture in the Si_3N_4 at the centre of the recess (Fig. 2c). This is then opened by CF_4 plasma etching. Subsequently, a Ti/Au layer is evaporated as the n-contact (and bonding) metal. The result is a small contact area (>100 nm^2) between the n and p regions at the centre of the pyramid for the µLED, all achieved by exploiting self-aligning processes and without sophisticated high-resolution lithography. To prepare for substrate removal the sample is bonded onto another Ti/Au-coated GaAs substrate with the assistance of an Sn–Au ribbon via a reflow soldering process, which provides a large-area contact.

Electroluminescence

Once the section of the wafer patterned with pyramidal recesses had been fully processed, all of the pyramids were contacted by evaporating a thin semitransparent layer of titanium (1 nm) and gold (20 nm), and bonding a Kapton insulated wire to the whole structure.
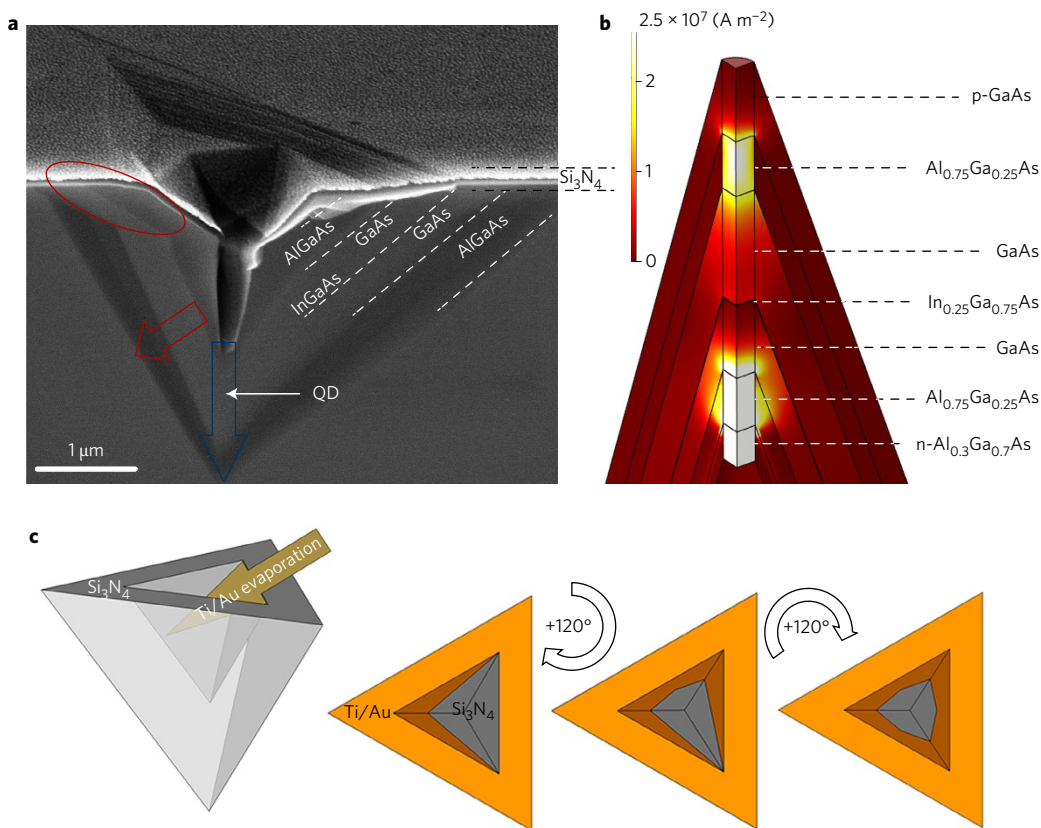
Figure 2 | Selective injection scheme and its realization. a, Scanning electron microscopy image of the cross-section of an epitaxial layer structure grown within a pyramidal recess; the device is cleaved in half and still contained within the GaAs substrate in the initial, apex-down, geometry. The contrast between the layers is mostly due to the different alloy compositions. A blue (red) arrow shows the preferential (most probable) direction of carrier injection. The region with irregular growth facets close to the surface, which could lead to current leakage/shortcut, is encircled in red. The top of the sample is covered with Si_3N_4, except for the central part of the pyramid where the back contact of a μLED is formed. **b**, Colour map of the current density in a simulated pyramidal structure (see Methods). The current density is concentrated in the regions of the vertical quantum wires (VQWRs). **c**, The steps in the fabrication process that form an aperture within the Si_3N_4 at the central part of the pyramidal recess. Ti/Au (3/15 nm) is evaporated at an angle so that the configuration of the recess would be partially shadowing gold deposition, as depicted in the left corner. By rotating the sample by 120° twice more and repeating the evaporation process, an open Si_3N_4 area is left, which is etched away with a CF_4 plasma, exploiting the Au layer as a protecting mask.

At this stage, for simplicity, all μLEDs are contacted, and all potentially turn on. An example (Sample A; see Methods and Supplementary Information for a detailed sample description) of gradually turning-on all (~1,300) contacted μLEDs at 10 K is shown in Fig. 3c. The bright spots of spectrally unfiltered integrated electroluminescence match the initial pyramidal recess pattern, demonstrating that each individual pyramid turns on without significant leakage through the GaAs substrate. This is confirmed by a macro-electroluminescence spectrum in Fig. 3b, where the dominant luminescence features at a high injection current of 4 mA are the InGaAs LQWR and LQWS, which clearly exceed the QD luminescence and are easily observable using a regular CCD imaging camera. The non-uniformity of intensity regions reflects differences between individual μLEDs as each of them turn on at slightly different voltages—the I–V curve shown in Fig. 3a is characteristic of the whole ensemble and not of a single device. However, we stress that there is no obstacle to selecting individual or a specific subset of μLEDs in future experiments to address or drive them independently, as this would not require any refinement in the processing of the device.

Several phenomena may be contributing to the inhomogeneity of the electric injection properties: (1) an inhomogeneous etching profile during the BE step, (2) a complex non-planar surface profile of the back contact side due to slightly irregular MOVPE growth towards the centre of the pyramid, which tends to close the recess irregularly creating variable conditions for the back-contact

formation, and (3) the presence of resistance at the contact side (most probably the p-doped side). These phenomena explain why the turn-on voltage is unexpectedly high, around 7 V, as shown by a three-dimensional colour map (Fig. 3d) of the dependence of the electroluminescence of a representative QD (Sample B1) on the driving voltage, where the dominant transitions are a negative trion (X-), exciton (X) and biexciton (XX). We estimate the overall extraction efficiency from these structures with the present design to be around 1% (see Methods for more details).

The average linewidth of exciton and biexciton transitions was found to be 138 ± 34 μeV and 97 ± 23 μeV, respectively. Although practical applications will require transform-limited linewidth photons, we argue that the broadening is not a fundamental issue here. It is mostly related to a 'charged' vicinity of the QDs inducing spectral wandering[24]. We observe that, at this scale of broadening, the external electric field that drives the device has no substantial effect. One of the clearly demonstrated sources of charge noise in this QD system is the deep hole trapping levels in the barriers[18]. The origin of the charge trapping states is most likely to be related to the processing-induced defects and MOVPE reactor state. We would like to stress that this can be overcome, and that we have a number of successfully fabricated samples with a high density of QDs with resolution-limited (<18 μeV) linewidth transitions under optical excitation[25]. As we will show, spectral wandering (a relatively slow process compared with the timescale of the
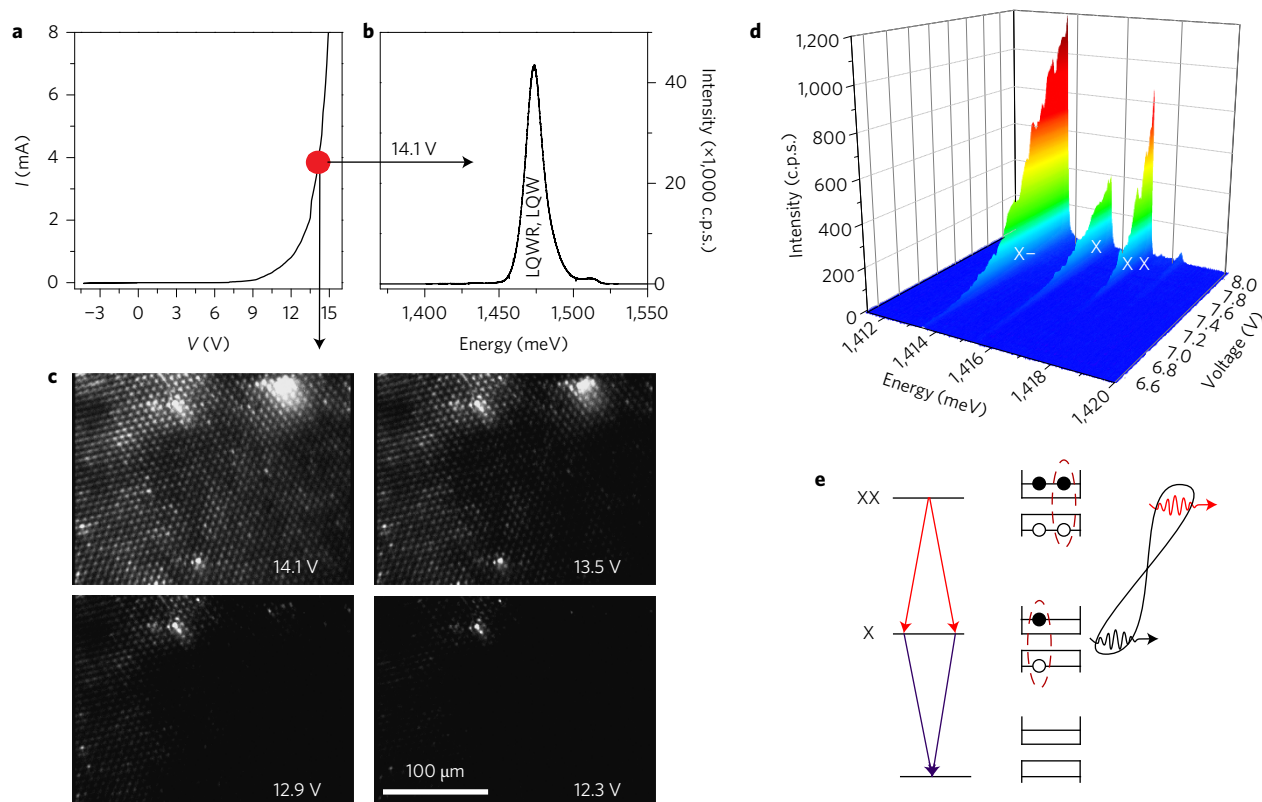
Figure 3 | Electroluminescence of µLEDs. a, *I–V* curve of Sample A taken at 8 K. The arrows point to the electroluminescence spectrum and the optical image obtained at 14.1 V indicated by the red dot on the *I-V* curve. **b**, Macro-electroluminescence spectrum taken under an applied bias voltage of 14.1 V. The dominant features are the LQWRs and LQWs. **c**, Optical images of switching on µLEDs with increasing applied bias. The light is not spectrally filtered. **d**, Dependence of the electroluminescence intensity (counts per second) on the applied voltage for a single QD (Sample B1). The three dominant transitions are a negative trion (X−), exciton (X) and biexciton (XX). **e**, Polarization-entanglement realization scheme with XX and X transitions shown by arrows. The biexciton is composed of two electrons and two holes (two excitons) and is described by a singlet-like state. In the shown scheme, an electron (a hole) is presented as a black (white) circle. Their complex, an exciton, is outlined by a dashed oval. During the recombination cascade through the intermediate exciton state, a pair of polarization-entangled photons shown by wavy arrows is emitted.

biexciton–exciton recombination cascade) does not preclude a high fidelity of entanglement.

Polarization-entangled photon emission

A QD initially populated by the electronic biexciton state (two electrons and two holes, a 'singlet-like' configuration) fully recombines through the intermediate state exciton (one electron and one hole) emitting two successive photons that are polarization-entangled (Fig. 3e)[26,27]. Provided that the recombination process proceeds coherently, and that the QD has symmetric carrier confinement potential, the emitted pair of photons is described by the Bell state $|\psi\rangle = (1/\sqrt{2})(|H_{XX}H_X\rangle + |V_{XX}V_X\rangle)$, where $|H\rangle$ and $|V\rangle$ are horizontal and vertical polarization states. However, QD symmetry is very rarely achieved[28–30]—electron–hole exchange interactions lift degeneracy in the exciton level by an amount of energy known as the fine-structure splitting (FSS), which causes beating (coherent oscillations) of the exciton spin state[18,31,32] and is later transferred to the two-photon polarization state. Integration over many photon-pair emission-detection events degrades or completely eliminates entanglement if the events are not temporally resolved. The reduction of FSS to the needed sub-microelectronvolt level can be achieved either through various external tuning strategies[31,33–35] or by exploiting intrinsic growth properties[11,36], as done in this work.

Figure 4a shows a map of a randomly selected area to measure the density of functional µLEDs with bright X and XX transitions and the distribution of the FSS values, where filled-in triangles represent emitting µLEDs. Dysfunctional QDs (represented by open

triangles) were either strongly charged or non-emitting due to possible defects in the vicinity of a QD. The numbers inside the triangles are the measured FSS values. Most of them are smaller than 4 µeV—in good agreement with previously found values from optically excited samples[18]. The full distribution of FSS values obtained from 94 µLEDs is shown in Fig. 4b; the average value is 2.9 ± 1.8 µeV, whereas the standard deviation of the exciton transition energy is 2.6 meV.

Two µLEDs with FSS values of 0.7 and 0.4 µeV (marked by a red border in the map in Fig. 4a) that were not subject to strong background electroluminescence from adjacent devices were selected to test for polarization entanglement. Six polarization-resolved biexciton–exciton continuous-wave (CW) injection intensity correlation curves that were measured in rectilinear, diagonal and circular bases are shown in Fig. 4c from a device with a FSS value of 0.4 ± 0.8 µeV. Clear correlations between co-polarized biexciton and exciton photons in rectilinear and diagonal bases, and anticorrelation in circular bases, are expected for polarization-entangled photons with a state $(1/\sqrt{2})(|HH\rangle + |VV\rangle)$, which is equivalent to $(1/\sqrt{2})(|DD\rangle + |AA\rangle) = (1/\sqrt{2})(|RL\rangle + |LR\rangle)$, where $|R\rangle = (1/\sqrt{2})(|H\rangle + i|V\rangle)$, $|L\rangle = (1/\sqrt{2})(|H\rangle + i|V\rangle)$, $|D\rangle = (1/\sqrt{2})(|H\rangle + |V\rangle)$ and $|A\rangle = (1/\sqrt{2})(|H\rangle + |V\rangle)$ are the right/left-hand circular, diagonal and antidiagonal polarization states, respectively. The calculated fidelity curve (see Methods) is shown in the bottom graph of Fig. 4c. By selecting correlation events around 0 ns delay from the time window of 0.5 ns, the fidelity value was found to be 0.73 ± 0.06, exceeding the classical limit of 0.5. The fidelity to the
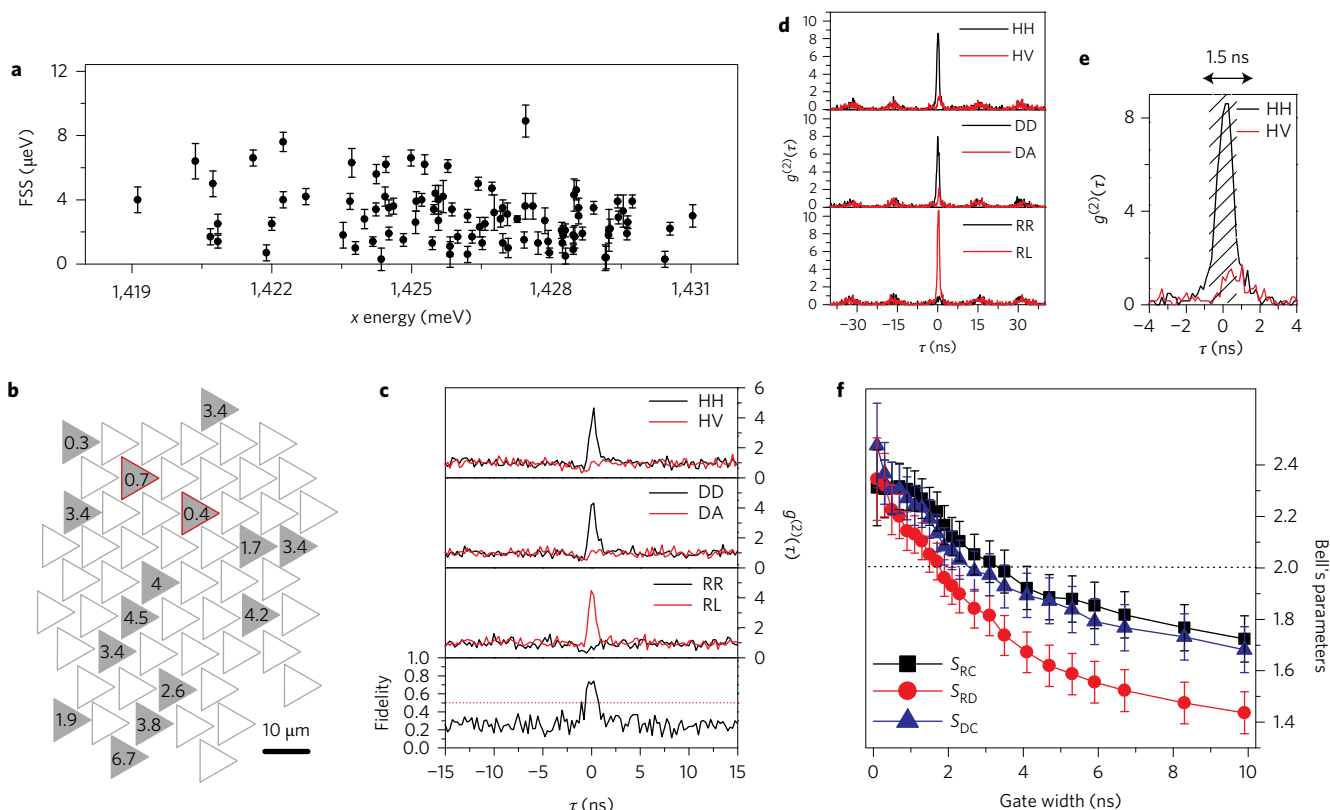
Figure 4 | Measurements of two-photon polarization state entanglement. a, Distribution of exciton FSS values obtained from Sample B2. The error bars represent the standard deviation from a fitted sinusoid curve (see Methods). **b,** Map of μLEDs from a randomly selected area. Grey triangles represent working devices with unquestionable exciton–biexciton emission. The numbers inside the triangles are the FSS values. Two devices framed in red and with FSS values of 0.7 and 0.4 μeV emitted polarization-entangled photons. **c,** The top three plots show polarization-resolved the second-order correlation function $g^{(2)}$ dependence on the delay (τ) between biexciton and exciton detection moments. The curves were obtained under continuous-wave excitation in linear, diagonal and circular polarization bases from a device with a FSS value of 0.4 μeV. The calculated curve of the fidelity to the expected maximally entangled state is shown in the bottom graph. The classical limit of 0.5 is significantly exceeded around 0 ns delay. **d,** Polarization-resolved second-order correlation curves taken in rectilinear, diagonal and circular polarization bases under pulsed μLED current injection. **f,** Three Bell's parameters calculated by a simplified procedure using the results shown in **e**. By selecting correlation events from a time-window of 1.5 ns and preserving 75% of the initial intensity, all three parameters violated the classical limit of two (dotted line), proving the non-classical nature of the polarization state. The error propagation to the values of all parameters has been estimated using Poissonian uncertainty.

expected maximally entangled state of photons emitted from a μLED QD with FSS of 0.7 ± 0.5 μeV in close proximity was found to be 0.69 ± 0.06.

Practical applications will require a triggered source of photons, where ideally a single pair of polarization-entangled photons would be generated on demand. Sample B1 was therefore injected with a pulsed current with a 63 MHz repetition rate (see Methods). Polarization-resolved second-order correlation curves obtained from a QD with an FSS value of 0.2 ± 0.2 μeV are shown in Fig. 4d. The expected correlations and degree of entanglement, as quantified by the fidelity value $f = 0.678 ± 0.023$, confirmed the non-classical state of the photons. While the FSS value of this representative QD is small enough to have a substantial effect on entanglement degradation, several other phenomena contribute. Among them are a finite pulse-width of the current (1.4 ns), which causes partial repopulation of a QD, and a small background emission from the adjacent μLEDs. By using a time-gating technique, which could be defined as a selection of correlation events from a specific time window, the contribution of these phenomena can be significantly reduced. For example, by selecting events from a 1.5 ns window (shown in the inset of Fig. 4e) and preserving 75% of the total two-photon detection events, the fidelity increased to 0.823 ± 0.019 (with a shorter time window of 0.1 ns fidelity can reach 0.881 ± 0.042, but care needs to be taken as the photon statistics is also decreased). These correlation

measurements allow a simplified estimation of three Bell parameters, S_{RD}, S_{DC} and S_{RC} as defined in ref. 37, and which can be used in quantum communication protocols[38]. By selecting correlation events from a 1.5 ns window, the parameters were measured to be $S_{RD} = 2.053 ± 0.070$, $S_{DC} = 2.191 ± 0.075$ and $S_{RC} = 2.239 ± 0.074$, all violating Bell's inequalities.

Conclusions and outlook

In summary, we present a quantum photonics technology that could enable the fabrication of site-controlled, scalable arrays of electrically driven sources of polarization-entangled photons with high entanglement quality. The devices are lithographically positioned, compatible with compound semiconductor foundry technologies, and for this reason attractive candidates for integrated photonic circuits.

Nevertheless, work is needed to further improve our sources to achieve the maximum capability in the context of quantum information processing: achieving photon indistinguishability across all devices, external control of the remaining FSS and enhancing the photon extraction efficiency are among the top priorities. Strain, possibly combined with an electric field[12,39], is one of the most promising strategies for tuning the emission energy and FSS. This strategy already proved to be efficient in the first prototypes based on the pyramidal QD system. The distribution of the emission energy that is typically observed (standard deviation of 2.5–3 meV) in our sample(s)

could be easily corrected by these methods, delivering the same excitonic emission energies for each pyramid. Our short-term aims are to improve source tunability by implementing a six-legged semiconductor–piezoelectric device, as done in a previous study[40], and to achieve full control of the FSS associated with each pyramid. Another critical parameter—the transition linewidth, which is expected to be transform-limited—is subject to the electric (and magnetic) fields present in the vicinity of a QD[24], including the external electric field applied for device operation. However, this is not a fundamental limitation, as has already been demonstrated that electrically driven QD devices can emit photons with a linewidth close to the theoretical limit[41]. By optimizing the processes used in the growth and design/fabrication of the devices to minimize defect density and charge accumulation, high spectral purity is expected to be achieved. Indeed, a linewidth of a few microelectronvolts (resolution-limited) from non-resonantly optically excited pyramidal QDs was already demonstrated[25]. Finally, photon collection efficiency can be increased with proper on-chip lensing and waveguiding strategies[42–44], which potentially allow photon extraction efficiencies of up to 80%.

Methods

Methods and any associated references are available in the online version of the paper.

References

1. O'Brien, J. L., Furusawa, A. & Vučković, J. Photonic quantum technologies. *Nat. Photon.* **3,** 687–695 (2009).
2. Gisin, N. & Thew, R. Quantum communication. *Nat. Photon* **1,** 165–171 (2007).
3. Aspuru-Guzik, A. & Walther, P. Photonic quantum simulators. *Nat. Phys.* **8,** 285–291 (2012).
4. Ladd, T. D. *et al.* Quantum computers. *Nature* **464,** 45–53 (2010).
5. Michler, P. *et al.* A quantum dot single-photon turnstile device. *Science* **290,** 2282–2285 (2000).
6. Santori, C., Fattal, D., Vučković, J., Solomon, G. S. & Yamamoto, Y. Indistinguishable photons from a single-photon device. *Nature* **419,** 594–597 (2002).
7. Akopian, N. *et al.* Entangled photon pairs from semiconductor quantum dots. *Phys. Rev. Lett.* **96,** 130501 (2006).
8. Young, R. J. *et al.* Improved fidelity of triggered entangled photons from single quantum dots. *New J. Phys.* **8,** 29–29 (2006).
9. Hafenbrak, R. *et al.* Triggered polarization-entangled photon pairs from a single quantum dot up to 30 K. *New J. Phys.* **9,** 315–315 (2007).
10. Dousse, A. *et al.* Ultrabright source of entangled photon pairs. *Nature* **466,** 217–220, (2010).
11. Juska, G., Dimastrodonato, V., Mereni, L. O., Gocalinska, A. & Pelucchi, E. Towards quantum-dot arrays of entangled photon emitters. *Nat. Photon.* **7,** 527–531 (2013).
12. Trotta, R., Wildmann, J. S., Zallo, E., Schmidt, O. G. & Rastelli, A. Highly entangled photons from hybrid piezoelectric-semiconductor quantum dot devices. *Nano Lett.* **14,** 3439–3444 (2014).
13. Kuroda, T. *et al.* Symmetric quantum dots as efficient sources of highly entangled photons: violation of Bell's inequality without spectral and temporal filtering. *Phys. Rev. B* **88,** 041306(R) (2013).
14. Versteegh, M. A. M. *et al.* Observation of strongly entangled photon pairs from a nanowire quantum dot. *Nat. Commun.* **5,** 5298 (2014).
15. Boretti, A., Rosa, L., Mackie, A. & Castelletto, S. Electrically driven quantum light sources. *Adv. Opt. Mater.* **3,** 1012–1033 (2015).
16. Salter, C. L. *et al.* An entangled-light-emitting diode. *Nature* **465,** 594–597 (2010).
17. Zhang, J. *et al.* High yield and ultrafast sources of electrically triggered entangled-photon pairs based on strain-tunable quantum dots. *Nat. Commun.* **6,** 10067 (2015).
18. Juska, G. *et al.* Conditions for entangled photon emission from (111)B site-controlled pyramidal quantum dots. *J. Appl. Phys.* **117,** 134302 (2015).
19. Pelucchi, E. *et al.* Decomposition, diffusion, and growth rate anisotropies in self-limited profiles during metalorganic vapor-phase epitaxy of seeded nanostructures. *Phys. Rev. B* **83,** 205409 (2011).
20. Dimastrodonato, V., Pelucchi, E. & Vvedensky, D. D. Self-limiting evolution of seeded quantum wires and dots on patterned substrates. *Phys. Rev. Lett.* **108,** 256102 (2012).
21. Moroni, S. T. *et al.* Indium segregation during III–V quantum wire and quantum dot formation on patterned substrates. *J. Appl. Phys.* **117,** 164313 (2015).
22. Zhu, Q. *et al.* Alloy segregation, quantum confinement, and carrier capture in self-ordered pyramidal quantum wires. *Nano Lett.* **6,** 1036–1041 (2006).
23. Dimastrodonato, V., Mereni, L. O., Young, R. J. & Pelucchi, E. Growth and structural characterization of pyramidal site-controlled quantum dots with high uniformity and spectral purity. *Phys. Status Solidi B* **247,** 1862–1866 (2010).
24. Kuhlmann, A. V. *et al.* Charge noise and spin noise in a semiconductor quantum device. *Nat. Phys.* **9,** 570–575, (2013).
25. Mereni, L. O., Dimastrodonato, V., Young, R. J. & Pelucchi, E. A site-controlled quantum dot system offering both high uniformity and spectral purity. *Appl. Phys. Lett.* **94,** 223121 (2009).
26. Benson, O., Santori, C., Pelton, M. & Yamamoto, Y. Regulated and entangled photons from a single quantum dot. *Phys. Rev. Lett.* **84,** 2513–2516 (2000).
27. Moreau, E. *et al.* Quantum cascade of photons in semiconductor quantum dots. *Phys. Rev. Lett.* **87,** 183601 (2001).
28. Schliwa, A., Winkelnkemper, M. & Bimberg, D. Impact of size, shape, and composition on piezoelectric effects and electronic properties of In(Ga)As/GaAs quantum dots. *Phys. Rev. B* **76,** 205324 (2007).
29. Seguin, R. *et al.* Size-dependent fine-structure splitting in self-organized InAs/GaAs quantum dots. *Phys. Rev. Lett.* **95,** 257402 (2005).
30. Abbarchi, M. *et al.* Exciton fine structure in strain-free GaAs/Al$_{0.3}$Ga$_{0.7}$As quantum dots: extrinsic effects. *Phys. Rev. B* **78,** 125321 (2008).
31. Langbein, W. *et al.* Control of fine-structure splitting and biexciton binding in In$_x$Ga$_{1-x}$As quantum dots by annealing. *Phys. Rev. B* **69,** 161301(R) (2004).
32. Hudson, A. J. *et al.* Coherence of an entangled exciton-photon state. *Phys. Rev. Lett.* **99,** 266802 (2007).
33. Bennett, A. J. *et al.* Electric-field-induced coherent coupling of the exciton states in a single quantum dot. *Nat. Phys.* **6,** 947–950 (2010).
34. Plumhof, J. D. *et al.* Strain-induced anticrossing of bright exciton levels in single self-assembled GaAs/Al$_x$Ga$_{1-x}$As and In$_x$Ga$_{1-x}$As/GaAs quantum dots. *Phys. Rev. B* **83,** 121302(R) (2011).
35. Trotta, R. *et al.* Universal recovery of the energy-level degeneracy of bright excitons in InGaAs quantum dots without a structure symmetry. *Phys. Rev. Lett.* **109,** 147401 (2012).
36. Karlsson, K. F. *et al.* Fine structure of exciton complexes in high-symmetry quantum dots: effects of symmetry breaking and symmetry elevation. *Phys. Rev. B* **81,** 161307(R) (2010).
37. Young, R. J. *et al.* Bell-inequality violation with a triggered photon-pair source. *Phys. Rev. Lett.* **102,** 030406 (2009).
38. Ekert, A. K. Quantum cryptography based on Bell's theorem. *Phys. Rev. Lett.* **67,** 661–663 (1991).
39. Zhang, J. *et al.* Electric-field-induced energy tuning of on-demand entangled-photon emission from self-assembled quantum dots. Preprint at: https://arxiv.org/abs/1604.04501 (2016).
40. Trotta, R. *et al.* Wavelength-tunable sources of entangled photons interfaced with atomic vapours. *Nat. Commun.* **7,** 10375 (2016).
41. Stevenson, R. M. *et al.* Indistinguishable entangled photons generated by a light-emitting diode. *Phys. Rev. Lett.* **108,** 040503 (2012).
42. Ma, Y., Kremer, P. E. & Gerardot, B. D. Efficient photon extraction from a quantum dot in a broad-band planar cavity antenna. *J. Appl. Phys.* **115,** 023106 (2014).
43. Gschrey, M. *et al.* Highly indistinguishable photons from deterministic quantum-dot microlenses utilizing three-dimensional *in situ* electron-beam lithography. *Nat. Commun.* **6,** 7662 (2015).
44. Lindenmann, N. *et al.* Photonic wire bonding: a novel concept for chip-scale interconnects. *Opt. Express* **20,** 17667–17677 (2012).

Author contributions

T.H.C. fabricated the devices. G.J. and S.T.M. carried out optical characterization, data processing and analysis. A.P. undertook the theoretical calculations. A.G. grew the samples and operated the MOVPE system. E.P. conceived the study and participated in its design and coordination. All authors commented on the final manuscript.

Additional information

Supplementary information is available in the online version of the paper. Reprints and permissions information is available online at www.nature.com/reprints. Correspondence and requests for materials should be addressed to G.J.

Competing financial interests

The authors declare no competing financial interests.

Methods

Sample growth. All of the presented results were obtained from the three samples referred to in the text as samples A, B1 and B2. The structures were grown by MOVPE on (111)B oriented GaAs substrates that were pre-patterned with tetrahedron recesses with a pitch of 7.5 μm for the sample A and 10 μm for samples B1 and B2. Among them, the samples with μLEDs that emitted entangled photons are B1 and B2, which were from an identical epitaxial structure but processed in different runs. The nominal QD composition and thickness of the latter samples are $In_{0.25}Ga_{0.75}As$ and 0.55 nm. The full epitaxial structure, doping and the role of each layer are given in the Supplementary Information.

μLED fabrication. The detailed steps for fabricating μLEDs are given in Supplementary Information.

Measurements. Measurements were taken at 10 K using a helium closed-cycle cryostat. Electroluminescence values were collected in a standard microphotoluminescence set-up using ×100 magnification and a 0.80 NA long-working-distance objective, which enabled a single device to be probed in each measurement.

The FSS measurements were taken using a combined multiple measurement and fitting procedure[37]. Linear polarization components were analysed by placing a polarizer in front of the monochromator and rotating a half-wave plate with a step of 1.5°. Exciton and biexciton transitions were fitted with Lorentzian fits; the corresponding peak centres were subtracted and the resulting data were fitted by a sinusoid curve with an amplitude equal to the FSS value (an example is given in Supplementary Information). The standard deviation was taken as an error.

Polarization-entanglement was measured by discriminating exciton and biexciton transitions with two monochromators acting as narrow bandpass filters. Polarization projections were selected by an appropriate orientation of half-(quarter-) wave plates with respect to the polarizing beam-splitters placed after the monochromators equipped with 950 grooves per millimetre gratings (transverse electrical/transverse magnetic diffracted intensity ratio ~1 at 877 nm). Fibre-coupled avalanche-photo diodes were used to detect intensity at a single photon level. In such configuration, two polarization-resolved, second-order correlation curves were measured simultaneously. The error propagation to $g^{(2)}$ and fidelity values has been estimated by using a Poissonian uncertainty.

In pulsed excitation mode, samples were injected by pulses shaped with a positive d.c. offset that was set slightly below the μLED injection threshold (typically a few volts), with superimposed pulses of 1.4 ns in width, reaching maximum voltage of 20 V and repetition rates between 63 and 80 MHz. A typical detection rate for polarization-entangled photon pairs in these experimental conditions was ~1,000 pairs per hour, with an overall estimated extraction efficiency from our structures of ~1%. The final counts are also affected by the ~1.4% efficiency of our micro-photoluminescence set-up and a broad non-Gaussian μLED emission profile.

Fidelity and calculation of the Bell parameters. The two-photon polarization state can be estimated by a quantum state tomography procedure[45] that allows the reconstruction of a density matrix ρ from a set of 16 intensity measurements. As the expected maximally entangled state $|\psi\rangle = (1/\sqrt{2})(|HH\rangle + |VV\rangle)$ is known, the procedure can be simplified by reducing the number of measurements, which allows only the density matrix elements necessary to calculate the fidelity $f = \langle\psi|\rho|\psi\rangle$ of the entangled state $|\psi\rangle$: $f = 1/4(1 + C_R + C_D - C_C)$ to be obtained, where C_R, C_D and C_C are degrees of correlations taken in rectilinear, diagonal and circular polarization bases[31,46]. The degree of correlation is defined as $C_{basis} = (g^{(2)}_{XX,X} - g^{(2)}_{XX,\bar{X}}/g^{(2)}_{XX,X} - g^{(2)}_{XX,\bar{X}})$, where $g^{(2)}_{XX,X(\bar{X})}$ is the second-order correlation function with XX(X) being the polarization of a biexciton (exciton) and $\bar{X}$ being the orthogonal polarization of an exciton. A fidelity value greater than 0.5 is a quick indicator of entanglement.

The degrees of correlation C_R, C_D and C_C are used to calculate the simplified Bell parameters, S_{RD}, S_{DC} and S_{RC} as reported in ref. 37. Without ruling out local hidden-variable theories, the traditional CHSH form[47] of the inequality obtained from the measurements with four different combinations of polarizers can be simplified and expressed as $S_{RD} = \sqrt{2}(C_R + C_D) \leq 2$. Two further Bell parameters are calculated and known as $S_{DC} = \sqrt{2}(C_D + C_C) \leq 2$ and $S_{RC} = \sqrt{2}(C_R - C_C) \leq 2$.

Current density simulations. Finite element simulations were performed using COMSOL Multiphysics 5.0. The simulations were obtained by solving Poisson's equation in conjunction with the continuity equations to calculate the voltage and carrier density (electrons and holes) in a 2D geometry (described below). Rotational symmetry along the vertical direction was applied to confer a 3D structure to the simulated geometry and to improve the approximation to the real pyramidal structure. The 2D geometry consisted of half of the cross-section of a regular triangular pyramid with sides of 7 μm in length cut along the centre of a face. The vertical wire in the centre of the 3D geometry was approximated to a cylinder with diameter of 100 nm. The simulated structure has seven internal layers that are (starting from the top layer in Fig. 1d): GaAs (60 nm thick), $Al_xGa_{1-x}As$ ($x = 0.75$, 45 nm thick), GaAs (90 nm thick), $In_{0.25}Ga_{0.75}As$ (1 nm thick), GaAs (60 nm thick), $Al_xGa_{1-x}As$ ($x = 0.75$, 45 nm thick) and finally $Al_xGa_{1-x}As$ ($x = 0.3$, 30 nm thick). In the vertical quantum wire the Al concentrations in the different layers were reduced to include segregation effects[19]: $x = 0.3$ was substituted with $x = 0.05$ and $x = 0.75$ was substituted with $x = 0.26$. The top layer was p-doped to a concentration of 1×10^{18} cm^{-3} and the external surface was set at constant voltage of 1.5 V. The bottom layer was n-doped to a concentration of 1×10^{18} cm^{-3} and set at ground. The current density (J) values reported in Fig. 1d are the nodal values calculated from the electric field distribution E and the conductivity σ using the relation $J = \sigma E$.

References

45. James, D. F. V., Kwiat, P. G., Munro, W. J. & White, A. G. Measurement of qubits. *Phys. Rev. A* **64,** 052312 (2001).
46. Shields, A. J., Stevenson, R. M. & Young, R. J. in *Single Semiconductor Quantum Dots* (ed. Michler, P.) 227–265 (Springer, 2009).
47. Clauser, J. F., Horne, M. A., Shimony, A. & Holt, R. A. Proposed experiment to test local hidden-variable theories. *Phys. Rev. Lett.* **23,** 880–884 (1969).